Journal of Alloys and Compounds 748 (2018) 163–170

Contents lists available at ScienceDirect

Journal of Alloys and Compounds

journal homepage: http://www.elsevier.com/locate/jalcom

Nanotwins induced by pulsed laser and their hardening effect in a Zr alloy

Linjiang Chai [a, *], Ke Chen [a], Yan Zhi [a], Korukonda L. Murty [b], Liang-Yu Chen [c, **], Zhinan Yang [d]

[a] College of Materials Science and Engineering, Chongqing University of Technology, Chongqing, 400054, China
[b] Department of Nuclear Engineering, North Carolina State University, Raleigh, NC 27695-7909, USA
[c] School of Science, Jiangsu University of Science and Technology, Zhenjiang, Jiangsu 212003, China
[d] National Engineering Research Center for Equipment and Technology of Cold Strip Rolling, Yanshan University, Qinhuangdao, 066004, China

ARTICLE INFO

Article history:
Received 6 December 2017
Received in revised form
19 February 2018
Accepted 10 March 2018
Available online 13 March 2018

Keywords:
Zr alloy
Pulsed laser
Nanotwins
Hardening
Electron backscatter diffraction

ABSTRACT

A pulsed laser was employed to treat a Zr-2.5Nb alloy with laser-induced microstructures (especially dense nanotwins) characterized by electron channeling contrast imaging (ECC) imaging and electron backscatter diffraction (EBSD) techniques. Hardening effect of the nanotwins was derived by analyzing hardness contributions from various microstructural factors modified by the pulsed laser treatments (PLT). Results show that dense nanotwins, that are difficult to introduce into Zr alloys by conventional thermo-mechanical methods, can be readily produced by the PLT at laser powers of 50 and 100 W. The twinning system is determined to be the compressive type of {10−11}⟨10−12⟩ by orientation analyses using EBSD. After the PLT, specimen hardness is markedly increased, which could be attributed to not only grain refinement and solid solution of Nb but more considerably to the abundance of the {10−11} nanotwins, demonstrating their strong hardening effect.

1. Introduction

In recent years, nanotwins have received wide and ever-increasing interests from both academia and industries because of their demonstrated superiority in enhancing mechanical properties of structural metallic materials [1,2]. To obtain high density of nanotwins, various materials processing techniques have been attempted by different research groups with effective methods including electro-deposition, dynamic plastic deformation, surface mechanical attrition treatment, etc [3]. It is to be noted that such attractive nanotwins have to-date been mainly found and studied in metals with a cubic structure such as Cu and austenitic stainless steel [4,5]. Most methods working well for introducing nanotwins into cubic metals are found to be less effective after applying to hexagonal-close-packed (hcp) metals [1]. As a consequence, dense twins have relatively rarely been observed in nanostructured hcp materials although twinning is well-known to play a crucial role in deforming their coarse-grained counterparts [6].

Zr alloys with hcp α phase at room temperature have important structural applications in chemical and nuclear industries owing to excellent corrosion resistance and nuclear properties [7–10]. Earlier studies revealed that extensive twinning activities can be observed in α-Zr deformed under specific conditions (favorable initial texture [11–13], low temperature [12,14,15], high strain rate [13,15–17], large grain [15,18], etc). However, twins in all these reports are found to have (sub-) microscale thicknesses, much thicker than that of desirable nanotwins. In contrast with the difficulty of producing dense nanotwins in α-Zr through conventional thermo-mechanical processing, our recent work showed that they could be obtained in a commercially pure Zr with pulsed laser surface treatments [19]. More attentions should be received by the pulsed laser-induced nanotwins to better reveal their specific characteristics and effects on properties.

In the present work, a Zr-2.5Nb alloy was subjected to the pulsed laser treatments (PLT) at two different powers, with microstructures containing abundant nanotwins expected to be produced. Detailed microstructural characterization for the nanotwins was then performed by electron channeling contrast (ECC) imaging and electron backscatter diffraction (EBSD) techniques. Based on the experimental results, origin and hardening effect of the PLT-

* Corresponding author.
** Corresponding author.
E-mail addresses: chailinjiang@cqut.edu.cn (L. Chai), lychen@just.edu.cn (L.-Y. Chen).

https://doi.org/10.1016/j.jallcom.2018.03.126
0925-8388/

induced nanotwins were analyzed and discussed.

2. Experimental

An as-received hot-deformed (forged to a strain of ~30%) Zr-2.5 wt% Nb alloy was selected as the starting material, with its melting point estimated as ~1800 °C. Rectangular specimens with the dimension of 3 mm × 8 mm × 15 mm along thickness, width and length directions (denoted as TD, WD and LD, respectively) were cut from the as-received Zr alloy material. LD-WD surfaces of the as-cut specimens were chemically cleaned using a mixed solution of 10 vol% hydrofluoric acid, 45 vol% nitric acid and 45 vol% distilled water and then subjected to pulsed laser irradiation (with the beam parallel to the TD) by use of a pulsed 600W Nd: YAG laser device. During the PLT, the irradiated areas were protected by continuously blown Ar gas to prevent oxidation. Two laser powers (50 and 100 W) were used in this work, with corresponding power densities of 63.7 and 127.4 W/mm^2, and energy densities of 6.3 and 12.5 J/mm, respectively. Other treatment parameters were kept the same: pulse duration 5 ms, pulse frequency 20 Hz, beam diameter 1 mm, defocusing amount +2 mm and beam travel speed 8 mm/s along the LD (throughout the specimen length).

A Zeiss Sigma HD field emission gun scanning electron microscope (FEGSEM) was used to investigate microstructural characteristics induced by the laser surface treatment. For direct microstructural observation, ECC images of backscattered electrons were taken, with demonstrated ability to reveal various crystallographic orientation-related defects like nanotwins [19–21]. For quantitative orientation analyses, on the other hand, an EBSD system with a NordlysMax^2 detector attached to the FEGSEM was utilized. Both the ECC and the EBSD examinations were performed on TD-WD surfaces (normal to the travel direction of the laser beam) of the specimens, with their preparation procedures already detailed elsewhere [22]. Hardness measurements were also made using a Vickers indentation tester (HVS-1000) for the as-received and the laser-treated specimens, with indentations located near the beam center in the latter ones (on the LD-WD surfaces). At least ten measurements were carried out for each specimen to calculate an average value. For each measurement, the applied load was 0.98 N (100 g) with a dwell time of 10 s.

3. Results

3.1. Microstructural characteristics

An ECC image of the as-received material is shown in Fig. 1a, from which a dual-phase microstructure consisting of bulk α grains and thin β films can be seen. The co-existence of α-Zr and β-Zr is also confirmed after performing EBSD indexing for both of them, as shown in Fig. 1b. For the α phase, varied contrasts in Fig. 1a suggest differences in their grain orientations due to the electron channeling effect [20]. On the other hand, the β films (~10% in volume fraction) are found to be always brighter compared to the α grains, which should be related to atomic number (Z) contrast of the backscattered electrons. Such a contrast effect enables a high-Z element to appear lighter than a low-Z element [23]. With respect to the case of Zr-Nb alloys, the atomic number of Nb ($Z_{Nb} = 41$) is slightly higher than that of Zr ($Z_{Zr} = 40$). It is thus known than the β phase is more Nb-enriched than the α phase in the as-received Zr-2.5Nb material, consistent with earlier reports [8,24]. In regards to phase dimensions, grain sizes of the α phase are found to spread from submicron to near ten micrometers while the β-film thicknesses limited to a few hundred nanometers. Average values of the α-grain size and the β-film thickness are measured to be about 1.4 μm and 72 nm, respectively. More specific orientation characteristics corresponding to the starting microstructure have been documented in our recent work [25].

Cross-sectional microstructures of the two PLTed specimens are presented in Fig. 2. Melting zones (MZs) of both the specimens are marked in Fig. 2a and b (low-magnification images). The maximum MZ widths of the 50 W and the 100 W specimens are measured to be about 850 and 1000 μm, respectively, with corresponding depths of 150 and 230 μm. This means that an increase of laser power is able to produce enlarged molten pools during laser irradiation. Closer observations (Fig. 2c and d) reveal that the MZs in both the laser-treated specimens are completely comprised of α-plate structures without any residual β phase. Most of these α plates are found to have submicron widths and their average value is determined by the linear intercept method to be about 290 nm in both the specimens. Clearly, remarkable α-grain refinements are induced by the PLT, compared to the starting microstructure. Additionally, after further magnified observations for the plate structures, a large number of small twins are found to extensively exist inside these plates (Fig. 2e and f). Measurements for such twins show that they essentially have lamellar thicknesses below a hundred nanometers, with the majority ranging from 30 to 70 nm. No evident difference is detected for sizes of the nanotwins in the specimens laser-treated at different powers. Nevertheless, their density seems to be slightly higher in the 100 W specimen. In consideration of the ultrafast cooling that can be induced by the PLT, the microstructures in the MZs are believed to correspond to twinned martensites. Also, the absence of β phase suggests

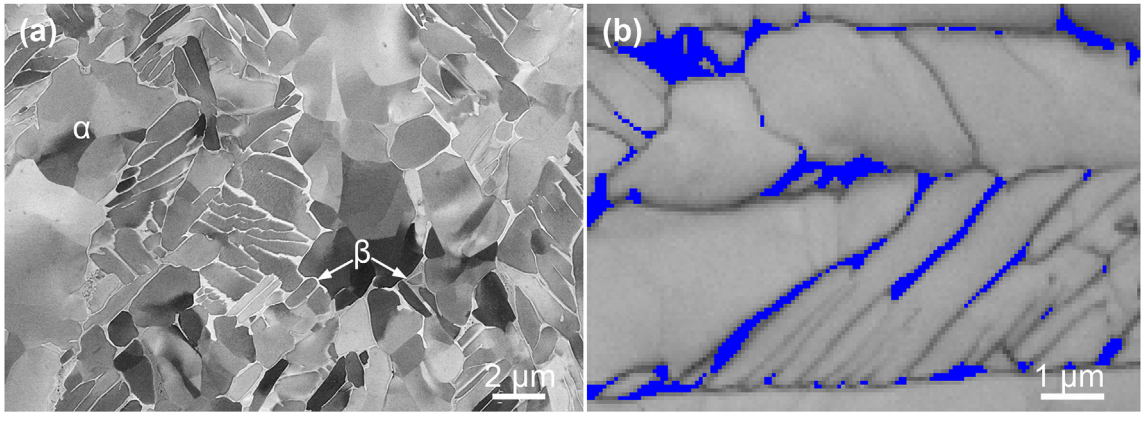

Fig. 1. The starting microstructure of the Zr-2.5Nb alloy: (a) ECC image and (b) EBSD band contrast map (step size 60 nm); the indexed β-Zr is colored blue in (b). (For interpretation of the references to color in this figure legend, the reader is referred to the Web version of this article.)

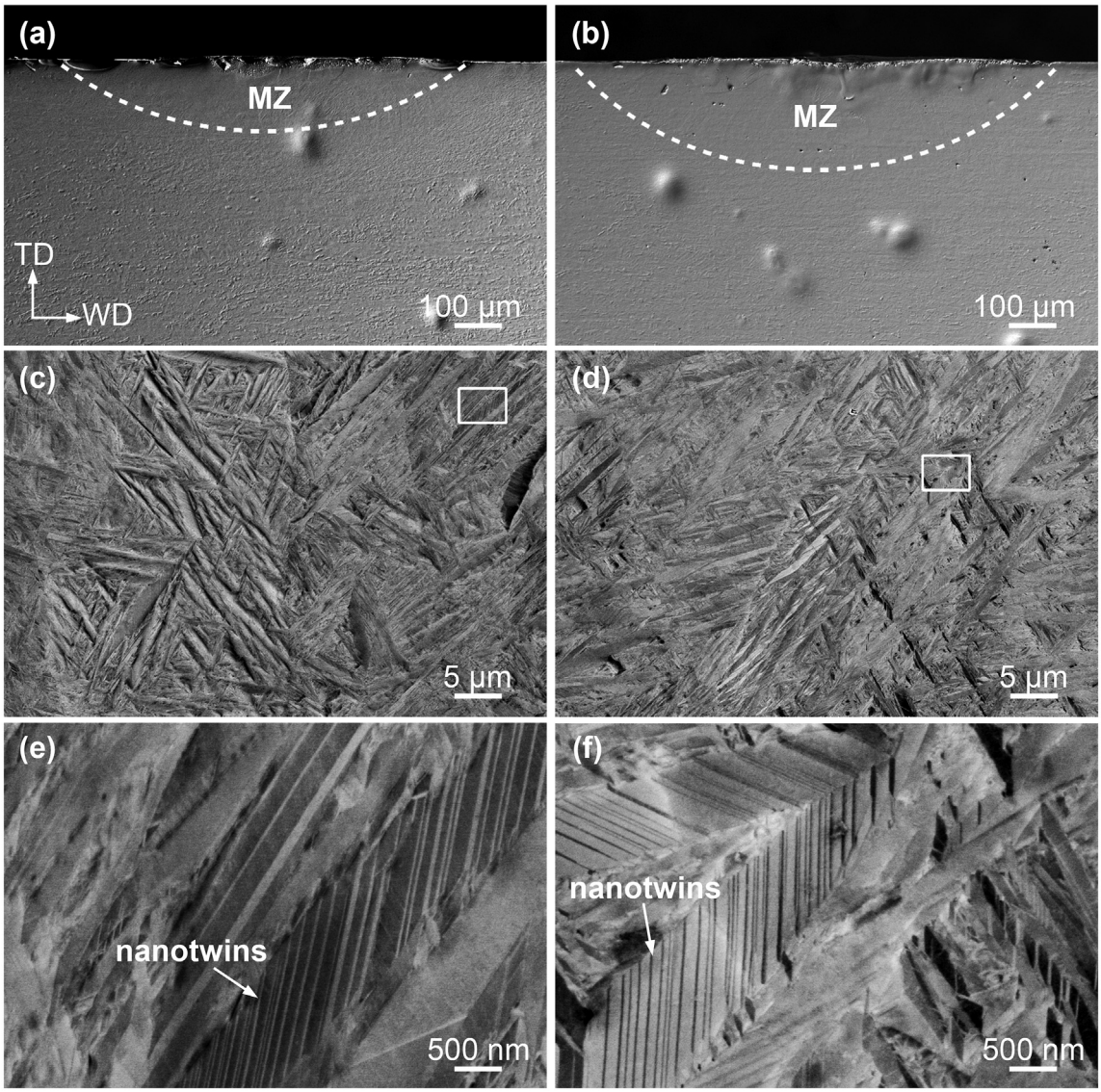

Fig. 2. Low-magnification cross-sectional observations of the 50 W (a) and the 100 W (b) specimens, with laser-melted zones roughly outlined by dashed lines; (c) and (d) typical microstructures in the MZ in (a) and (b), respectively; (e) and (f) significantly magnified images corresponding to boxed regions in (c) and (d), respectively.

completeness of the martensitic β→α transformation. Further measurements using more ECC images reveal that fractions of twinned α plates in the MZs of the 50 W and the 100 W specimens are about 77% and 83%, respectively.

EBSD scannings for typical regions in the MZs of both the laser-treated specimens are displayed and analyzed in Figs. 3 and 4. Fig. 3a is a band contrast (BC) map of the scanned region in the 50 W specimen, from which satisfactory image quality can be confirmed. Thanks to orientation sensitivity of Kikuchi diffraction patterns, nanotwins revealed in the ECC image (Fig. 2e) are also observable in the BC map, as marked in Fig. 3a. Nevertheless, as their thicknesses are close to or even smaller than the EBSD scanning step size, most of them show line-like appearances rather than lamellar morphologies (Fig. 3a). An inverse pole figure (IPF) map corresponding to Fig. 3a is presented in Fig. 3b, with black lines indicating high angle boundaries (HABs, $\theta > 15^\circ$). One can clearly see that most of the martensitic plates are separated with each other by HABs. Note that the Burgers orientation relationship (OR) [26] predicts five misorientation angles for boundaries between α products generated by the same β phase, i.e. 10.5°, 60°, 60.8°, 63.3° and 90° with specific rotation axes. Moreover, theoretical calculation shows that frequency of the four high angles around 60° and 90° should be above 90% [27]. This is consistent with results shown in Fig. 3c, from which the HABs in Fig. 3b can be confirmed to correspond to the Burgers misorientations (see their rotation axes as well). The Burgers OR is thus known to be well followed during the laser-induced martensitic β→α transformation.

In regards to the nanotwins observed in Fig. 3a, Fig. 3b shows that orientations of most of them cannot be successfully indexed and displayed in the IPF map, due mainly to their extremely small thicknesses. Nevertheless, success is fortunately reached for indexing a few thicker ones, allowing their orientation analyses to be quantitatively made. For example, misorientation angle variation across two twin lamellae (the arrow in Fig. 3b) is given in Fig. 3d. Results show that each twin boundary has a misorientation angle of about 57° with a rotation axis of ⟨11–20⟩. Such a misorientation characteristic suggests the nanotwins to be {10–11}⟨10–12⟩ compressive twins, with a theoretical angle/axis pair of 57.05°/⟨11–20⟩ with a parent grain in Zr alloys [28].

Similar characterization and analyses to Fig. 3 are also

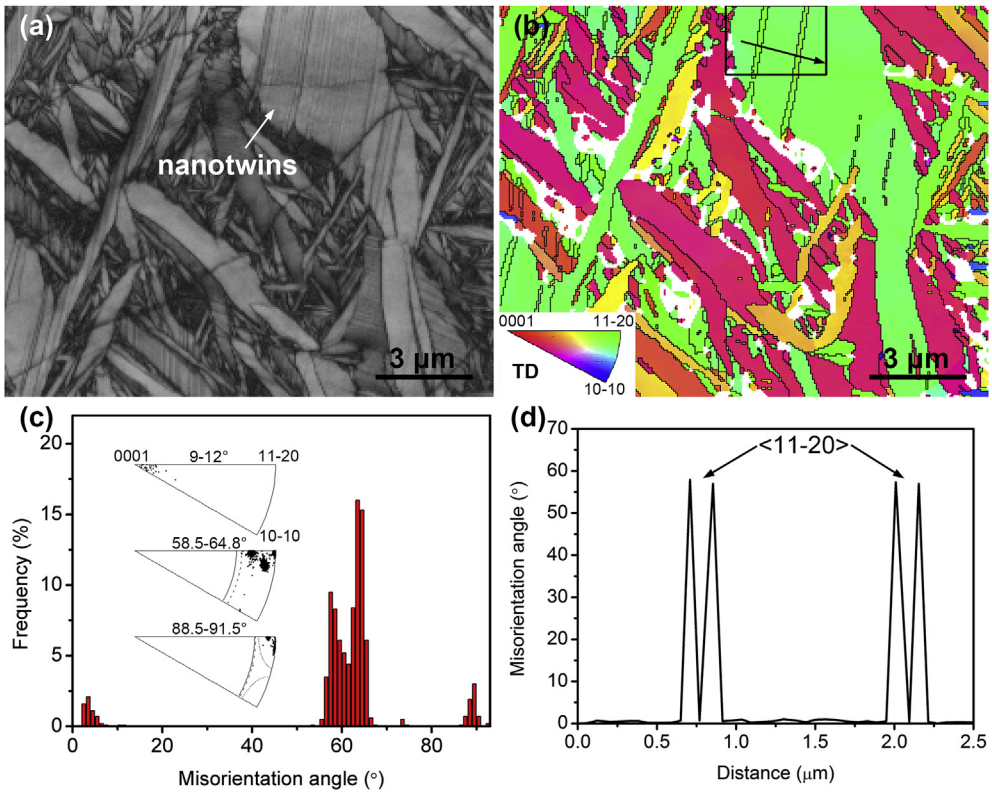

Fig. 3. EBSD characterization (step size 60 nm) for a selected region in the MZ of the 50 W specimen: (a) band contrast map, (b) inverse pole figure map with high angle boundaries represented by black lines, (c) misorientation angle and rotation axis distribution corresponding to (b), and (d) misorientation variation along the arrowed path in (b).

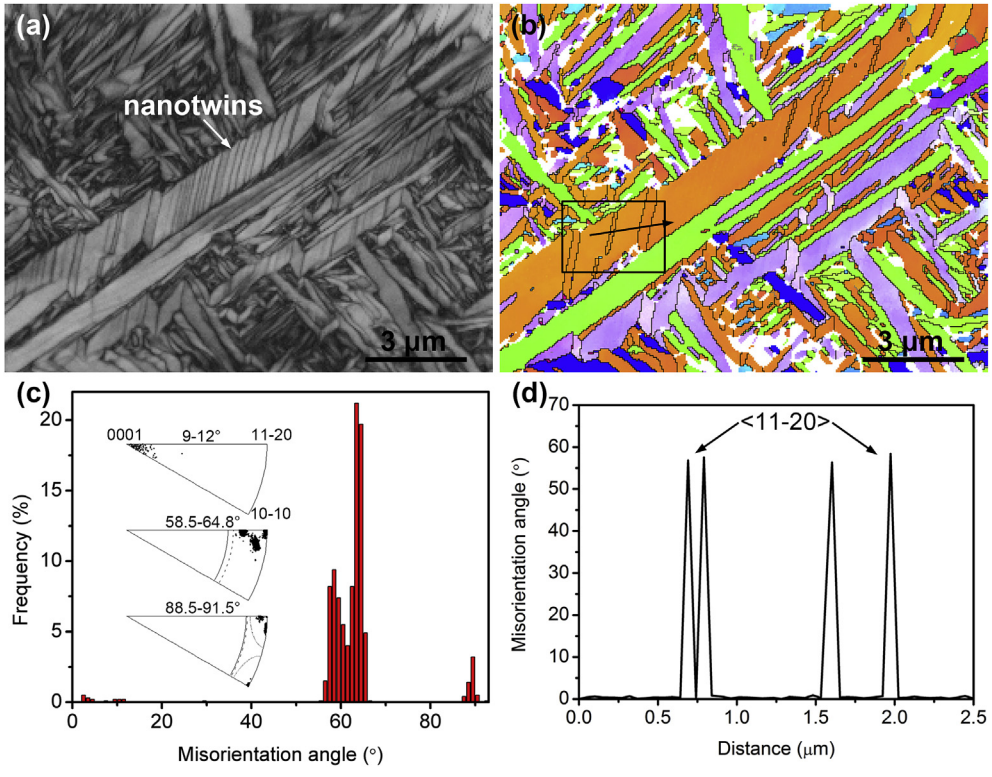

Fig. 4. EBSD characterization (step size 50 nm) for a selected region in the MZ of the 100 W specimen: (a) band contrast map, (b) inverse pole figure map with high angle boundaries represented by black lines, (c) misorientation angle and rotation axis distribution corresponding to (b), and (d) misorientation variation along the arrowed path in (b). The color code for Fig. 4b is the same as that indicated in Fig. 3b. (For interpretation of the references to color in this figure legend, the reader is referred to the Web version of this article.)

conducted for the 100 W specimen and presented in Fig. 4. From the BC map in Fig. 4a, the abundance of nanotwins can also be revealed. Misorientation angle and rotation axis characteristics of the α plates (Fig. 4b and c) are found to closely resemble those demonstrated in Fig. 3, indicating a similar transformation process. Fig. 4b shows that EBSD indexing of a few nanotwins is also achieved with their boundaries with the ~57°/⟨11–20⟩ misorientation as well (Fig. 4d).

To further verify the twinning system of the nanotwins, specific orientations of the twins and their parent grains (un-twinned parts) in selected regions are analyzed. Fig. 5a and c are orientation imaging maps with twins and parent grains extracted from the boxed regions in Figs. 3b and 4b, respectively. For each orientation, a schematic crystal in the specimen coordinate system is also displayed in Fig. 5a and c to facilitate stereographic understanding. Fig. 5b and d present pole figures of {10–11} and ⟨10–12⟩, which respectively correspond to habit plane and direction of the {10–11} twinning system. It is known that for two twin-related parts, projections of their habit planes and directions should completely coincide. One can observe from Fig. 5b that one of the six {10–11} planes of the twinning orientation is well coincident with that of their parent orientation. Meanwhile, exact coincidence also exists between one of their ⟨10–12⟩ directions. An identical projection feature can be noted in Fig. 5d. Hence, the nanotwins appeared in both the 50 W and the 100 W specimens can be firmly regarded to be {10–11} twins.

3.2. Hardness variation

Fig. 6 presents surface hardness variation induced by the PLT. For the as-received specimen, its average hardness is measured to be 222 ± 8 H V. The value is evidently increased by 73.6% to 385 ± 20 H V in the MZ of the 50 W specimen, suggesting a remarkable hardening effect for the PLT. For the 100 W specimen, the average hardness measured for its MZ is found to be further increased to 407 ± 21 H V, 83.5% higher than that of the as-received specimen. The hardnesses attained for the Zr-2.5Nb alloy in the present work are considerably higher than those (<300 H V) reported for such material after various conventional thermo-mechanical treatments in literature [8,29]. Also, the hardening effect induced by the PLT is stronger than that reached in a Zr-2.5Nb alloy treated by continuous wave CO_2 laser [30]. The hardening

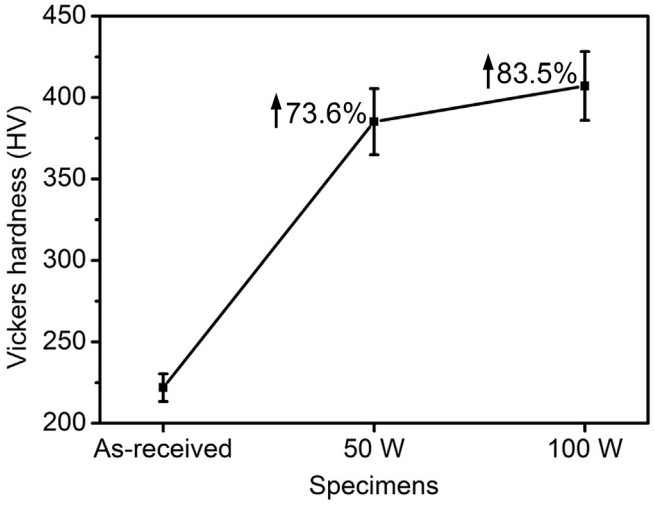

Fig. 6. Hardness variation induced by the pulsed laser treatments.

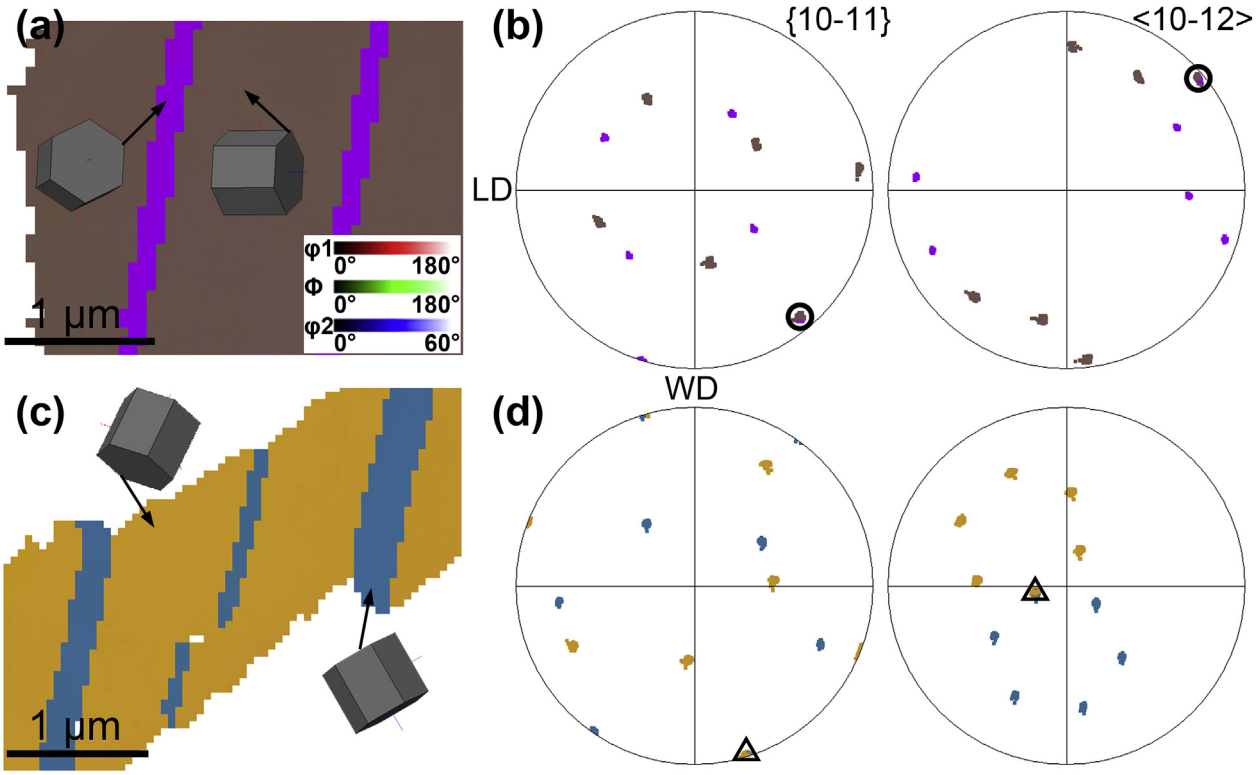

Fig. 5. (a) and (c) orientation imaging maps (reconstructed from all Euler angles) corresponding to boxed regions in Figs. 3b and 4b, respectively; (b) and (d) {10–11} and ⟨10–12⟩ pole figures corresponding to (a) and (c), respectively, with circle and triangle symbols indicating superposed projection. The color legend for (a) and (c) is shown in (a). (For interpretation of the references to color in this figure legend, the reader is referred to the Web version of this article.)

ability of the PLT is believed to be determined by the above-demonstrated microstructural characteristics (like nanotwins) and is discussed in the following.

4. Discussion

4.1. Origin of the nanotwins

As illustrated through Figs. 2–5, the microstructures in the MZs of both the PLTed specimens are fully comprised of fine martensitic plates with dense {10–11} nanotwins. For metallic materials, it is known that laser surface treatments allow selective melting of small volumes, followed by ultrafast quenching due to rapid heat extraction through the substrate [31]. With respect to Zr materials, a rapid phase transformation of liquid → β → α would occur during the laser surface irradiation. In recent work [32], the cooling rate reached in a PLTed commercially pure Zr (CP-Zr) was determined to be above 6000 °C/s, much higher than that induced by direct water quenching (~1000 °C/s). As a result of such rapid cooling, the PLT could even introduce a number of nanotwins into the CP-Zr [19,32], which was usually twin-free after β-water-quenching [26]. The addition of β-stabilizing elements (like Nb) into Zr alloys was reported to promote dislocation substructures inside martensitic plates to be replaced by small twins [33–35]. In fact, even by employing the conventional β-water-quenching, nanoscale twins have been observed inside some martensitic plates in Zr-2.5Nb alloy [36], in contrast with the twin-free case in the CP-Zr. Comparing both the PLTed CP-Zr [19] and Zr-2.5Nb alloy in the present work, much denser nanotwins can be noted in the latter one (Fig. 2) due probably to the 2.5 wt% Nb addition that could effectively lower the stacking fault energy of α-Zr [37]. The nanotwin density in the PLTed Zr-2.5Nb alloy is also clearly higher than that in β-water-quenched specimen [36], which can be attributed to the higher cooling rate.

In regards to the type of nanotwins, the {10–11} twinning system determined in this work is consistent with those primarily observed in twinned martensite in some Zr alloys [35,38,39]. During rapid martensitic transformation, there is inhomogeneous shear needed to be accommodated inside martensitic α plates. To this end, active dislocation slip and/or twinning are required, with the latter becoming preferred upon faster cooling. For various twinning systems operable in α-Zr, their twining shears are 0.104, 0.167, 0.225 and 0.63 for {10–11}, {10–12}, {11–22} and {11–21} twins, respectively [40]. In other words, the {10–11} twin exhibits the lowest twinning shear, which may account for its dominance over other twinning systems.

4.2. Hardening effect of the nanotwins

As shown in Fig. 6, remarkable hardening can be noted for the PLT-induced MZs. According to the above revealed microstructural features, the increased hardnesses could be attributed to several factors. Compared to the grain sizes (~1.4 μm on average) of the as-received specimen, the plate structures in the MZs of both the 50 W and the 100 W specimens are largely refined, with an average α-plate width of ~0.29 μm. In terms of the Hall-Petch equation, the hardness contribution from the grain refinement can be quantified as follows,

$$\Delta HV = k_{HP}^{H}\left(d_p^{-0.5} - d_0^{-0.5}\right), \quad (1)$$

where ΔHV is the hardness increment, k_{HP}^{H} is the Hall-Petch slope (in the unit of Vickers hardness), d_0 is the average grain size of the as-received specimen and d_p is the average plate width in the MZs. Using a Hall-Petch slope (200 MPa $\mu m^{1/2}$) reported for pure Zr [41], the k_{HV} is approximated to be 66.7 H V $\mu m^{1/2}$ (1/3 of that in the unit of MPa). By imputing the known values, the ΔHV is calculated to be about 68 H V according to Eq. (1). This corresponds to only a small part of the overall hardness increment (for example 385 H V − 222 H V = 163 H V for the 50 W specimen), suggesting that there must be other important contributors apart from the grain refinement.

After martensitic β→α transformation, alloying elements would usually be supersaturated in the matrix, leading to solid solution strengthening/hardening. In the MZs of the PLTed Zr-2.5Nb alloy, the disappearance of prior Nb-enriched β-Zr implies the supersaturation of Nb in the α plates. Since it is difficult to accurately measure the hardening effect of Nb in α-Zr, its solid-solution hardening contribution is tried to be indirectly estimated. In Ref. [42], a hardness value below 270 H V was reported for a β-water-quenched Zr-2.5Nb (solid-solution treated at 1000 °C) with a fully Nb-saturated martensitic microstructure. After comparing with that of the as-received specimen in this work, one notes that only limited hardening could be produced solely by the solid solution of 2.5 wt% Nb.

Other factors possibly contributing to hardening include dense dislocations and strong textures. With respect to dislocations, Figs. 3c and 4c reveal very limited numbers of LABs (dislocation boundaries) in the MZs. Moreover, average values of kernel average misorientations of the as-received, the MZs of the 50 W and the 100 W specimens are calculated (using EBSD data in Figs. 1, 3 and 4) to be 0.42°, 0.54° and 0.53°, respectively. Clearly, such values are relatively small and no significant differences exist between them, suggesting low dislocation densities and thus few hardness contributions by dislocations. As for textures, rather scattered orientations would be produced after rapid β cooling since many (exactly twelve) α orientations can be generated by one β orientation [26]. As a result, randomized textures could be expected for the MZs of the PLTed specimens (Figs. 3b and 4b), indicating minimal hardening contributions from phase transformation textures as well.

Besides the above factors, the dense nanotwins induced by the PLT are believed to be able to make a considerable contribution to hardening the MZs. Nanotwin boundaries have in recent years been well recognized as more effective barriers to dislocation slip than common grain boundaries in various metallic materials [43–45]. In fact, similar hardening due to such nanotwin boundaries has also been noticed in a CP-Zr [19]. To understand the specific role played by the {10–11} nanotwins presented in this work, the interaction of such twin boundaries with the easiest slip system ({10-10}⟨11–20⟩) in α-Zr can be considered. It was earlier figured out by Banerjee et al. [46] that two out of three variants of the prismatic slip cannot penetrate or slide along the {10–11} twin boundaries, demonstrating their effectiveness in resisting the dislocation movement. More generally, both molecular dynamics simulations [47] and experimental observations [45,48] revealed that for twins with nanoscale thicknesses, pile-ups of dislocations would no longer occur but be replaced by single-dislocation motion during deformation. An extremely high stress was then required to allow single dislocations to penetrate boundaries of the nanotwins, leading to strong strengthening and hardening. Note that nanotwin boundaries were also reported to be beneficial to increase the ductility of materials [45,49], which should be explored in the PLTed Zr alloys in the future work. One can now confirm that the majority of the hardness increment must have been contributed from the abundant {10–11} nanotwins in PLTed specimens. And the slightly higher hardness of the 100 W specimen (Fig. 6) could be ascribed to denser nanotwins in its MZ (Fig. 2), compared to that of the 50 W

specimen.

5. Conclusions

(1) The pulsed laser treatments (at 50 and 100 W) were demonstrated to be able to introduce dense nanotwins into Zr-2.5Nb alloy, as a result of shear accommodation during ultrafast $\beta \rightarrow \alpha$ cooling.
(2) The PLT-induced nanotwins were determined to correspond to the $\{10\bar{1}1\}\langle 10\bar{1}2\rangle$ twinning system.
(3) Significant hardening was reached by the pulsed laser treatments, which could be mainly attributed to the abundance of nanotwins, in addition to grain refinement and solid solution of Nb.

Acknowledgments

This work was financed by the National Natural Science Foundation of China (Grant Nos. 51401040, 51601075 and 51601165), the Scientific and Technological Research Program of Chongqing Municipal Education Commission (KJ1600924) and the Fundamental and Cutting-Edge Research Plan of Chongqing (cstc2017jcyjAX0114). One of us (KLM) acknowledges the support of the National Science Foundation grant CMMI 1727237. Critical comments from all the reviewers of this paper are gratefully appreciated.

References

[1] Y.T. Zhu, X.Z. Liao, X.L. Wu, Deformation twinning in nanocrystalline materials, Prog. Mater. Sci. 57 (2012) 1–62.
[2] K. Lu, L. Lu, Preface to the viewpoint set on the strengthening effect of nanoscale twins, Scripta Mater. 66 (2012) 835–836.
[3] K. Lu, Stabilizing nanostructures in metals using grain and twin boundary architectures, Nat Rev Mater 1 (2016) 16019.
[4] Y. Cao, Y.B. Wang, X.H. An, X.Z. Liao, M. Kawasaki, S.P. Ringer, T.G. Langdon, Y.T. Zhu, Concurrent microstructural evolution of ferrite and austenite in a duplex stainless steel processed by high-pressure torsion, Acta Mater. 63 (2014) 16–29.
[5] X.Z. Liao, Y.H. Zhao, S.G. Srinivasan, Y.T. Zhu, R.Z. Valiev, D.V. Gunderov, Deformation twinning in nanocrystalline copper at room temperature and low strain rate, Appl. Phys. Lett. 84 (2004) 592–594.
[6] J.L. Sun, P.W. Trimby, F.K. Yan, X.Z. Liao, N.R. Tao, J.T. Wang, Grain size effect on deformation twinning propensity in ultrafine-grained hexagonal close-packed titanium, Scripta Mater. 69 (2013) 428–431.
[7] L.Y. Chen, Q.F. Zeng, J.X. Li, J.Q. Lu, Y. Zhang, L.C. Zhang, X.J. Qin, W.J. Lu, L.F. Zhang, L.Q. Wang, D. Zhang, Effect of microstructure on corrosion behavior of a Zr-Sn-Nb-Fe-Cu-O alloy, Mater. Des. 92 (2016) 888–896.
[8] M. Zhang, F. Zhang, Z. Yang, Y. Li, L. Qu, H. Zhen, Effect of cooling process on the formation of duplex microstructure in Zr–2.3Nb alloy, J. Alloy. Comp. 651 (2015) 316–321.
[9] L. Chai, S. Wang, H. Wu, N. Guo, H. Pan, L. Chen, K.L. Murty, B. Song, $\alpha \rightarrow \beta$ Transformation characteristics revealed by pulsed laser-induced non-equilibrium microstructures in duplex-phase Zr alloy, Sci. China Technol. Sci. 60 (2017) 1255–1262.
[10] R. Kondo, N. Nomura, Y. Tsutsumi, H. Doi, T. Hanawa, Microstructure and mechanical properties of as-cast Zr–Nb alloys, Acta Biomater. 7 (2011) 4278–4284.
[11] R.J. McCabe, G. Proust, E.K. Cerreta, A. Misra, Quantitative analysis of deformation twinning in zirconium, Int. J. Plast. 25 (2009) 454–472.
[12] R.J. McCabe, E.K. Cerreta, A. Misra, G.C. Kaschner, C.N. Tome, Effects of texture, temperature and strain on the deformation modes of zirconium, Philos. Mag. A 86 (2006) 3595–3611.
[13] J.P. Escobedo, E.K. Cerreta, C.P. Trujillo, D.T. Martinez, R.A. Lebensohn, V.A. Webster, G.T. Gray III, Influence of texture and test velocity on the dynamic, high-strain, tensile behavior of zirconium, Acta Mater. 60 (2012) 4379–4392.
[14] G.C. Kaschner, C.N. Tomé, I.J. Beyerlein, S.C. Vogel, D.W. Brown, R.J. McCabe, Role of twinning in the hardening response of zirconium during temperature reloads, Acta Mater. 54 (2006) 2887–2896.
[15] S.G. Song, G.T. Gray, Influence of temperature and strain-rate on slip and twinning behavior of Zr, Metall. Mater. Trans. 26 (1995) 2665–2675.
[16] D.L. Zou, B.F. Luan, Q. Liu, L.J. Chai, J.W. Chen, Characterization of adiabatic shear bands in the zirconium alloy impacted by split Hopkinson pressure bar at a strain rate of 6000^{-1}, Mater. Sci. Eng. 558 (2012) 517–524.
[17] R. Kapoor, A. Sarkar, J. Singh, I. Samajdar, D. Raabe, Effect of strain rate on twinning in a Zr alloy, Scripta Mater. 74 (2014) 72–75.
[18] L. Chai, B. Luan, K.L. Murty, Q. Liu, Twinning during recrystallization cooling in α-Zr alloy, Mater. Sci. Eng. 576 (2013) 320–325.
[19] L. Chai, B. Chen, S. Wang, N. Guo, C. Huang, Z. Zhou, W. Huang, Microstructural changes of Zr702 induced by pulsed laser surface treatment, Appl. Surf. Sci. 364 (2016) 61–68.
[20] S. Zaefferer, N.-N. Elhami, Theory and application of electron channelling contrast imaging under controlled diffraction conditions, Acta Mater. 75 (2014) 20–50.
[21] L. Chai, B. Luan, B. Chen, H. Yang, Q. Liu, W. Huang, Concurrent inheritance of microstructure and texture after slow $\beta \rightarrow \alpha$ cooling of commercially pure Zr, Sci. China Technol. Sci. 59 (2016) 1771–1776.
[22] L. Chai, H. Wu, S. Wang, B. Luan, Y. Wu, X. Huang, Microstructural characteristics of cold-rolled Zr-2.5Nb alloy annealed near the monotectoid temperature, Sci. China Technol. Sci. (2017), https://doi.org/10.1007/s11431-017-9130-4.
[23] N. Guo, Q. Liu, Y. Xin, B. Luan, Z. Zhou, The application of back-scattered electron imaging for characterization of pearlitic steels, Sci. China Technol. Sci. 54 (2011) 2368–2372.
[24] P. Hovington, P.T. Pinard, M. Lagacé, L. Rodrigue, R. Gauvin, M.L. Trudeau, Towards a more comprehensive microstructural analysis of Zr–2.5Nb pressure tubing using image analysis and electron backscattered diffraction (EBSD), J. Nucl. Mater. 393 (2009) 162–174.
[25] L. Chai, S. Wang, B. Luan, Q. Liu, Electron backscatter diffraction investigation of duplex-phase microstructure in a forged Zr-2.5Nb alloy, Sci. China Technol. Sci. 59 (2016) 673–679.
[26] L. Chai, B. Chen, Z. Zhou, K.L. Murty, Y. Ma, W. Huang, A special twin relationship or a common Burgers misorientation between α plates after β quenching in Zr alloy? Mater. Char. 104 (2015) 61–65.
[27] C. Chauvy, P. Barberis, F. Montheillet, Microstructure transformation during warm working of beta-treated lamellar Zircaloy-4 within the upper alpha-range, Mater. Sci. Eng. 431 (2006) 59–67.
[28] E. Tenckhoff, Review of deformation mechanisms, texture, and mechanical anisotropy in zirconium and zirconium base alloys, J. ASTM Int. (JAI) 2 (2005) 25–50.
[29] Z.N. Yang, F.C. Liu, F.C. Zhang, Z.G. Yan, Y.Y. Xiao, Microstructural evolution and mechanical properties in Zr705 during the rolling process, Mater. Sci. Eng. 544 (2012) 54–58.
[30] K.F. Amouzouvi, L.J. Clegg, R.C. Styles, L. Mannik, T.-C. Ma, S.K. Brown, B.-W. Gu, Microstructural changes in laser hardened Zr-2.5Nb alloy, Scripta Metall. Mater. 32 (1995) 289–294.
[31] F. Weng, C. Chen, H. Yu, Research status of laser cladding on titanium and its alloys: a review, Mater. Des. 58 (2014) 412–425.
[32] L. Chai, B. Chen, S. Wang, Z. Zhou, W. Huang, Microstructural characteristics of a commercially pure Zr treated by pulsed laser at different powers, Mater. Char. 110 (2015) 25–32.
[33] Y.H. Jeong, K.O. Lee, H.G. Kim, Correlation between microstructure and corrosion behavior of Zr-Nb binary alloy, J. Nucl. Mater. 302 (2002) 9–19.
[34] D. Srivastava, P. Mukhopadhyay, S. Banerjee, S. Ranganathan, Morphology and substructure of lath martensites in dilute Zr-Nb alloys, Mater. Sci. Eng. 288 (2000) 101–110.
[35] H. Yang, S. Kano, Y. Matsukawa, Y. Li, J. Shen, F. Li, Z. Zhao, Y. Satoh, H. Abe, Effect of molybdenum on microstructures in Zr-1.2 Nb alloys after β-quenching and subsequently 873K annealing, Mater. Des. 104 (2016) 355–364.
[36] D. Srivastava, K. Madangopal, S. Banerjee, S. Ranganathan, Self accommodation morphology of martensite variants in Zr-2.5wt%Nb alloy, Acta Metall. Mater. 41 (1993) 3445–3454.
[37] Y. Udagawa, M. Yamaguchi, T. Tsuru, H. Abe, N. Sekimura, Effect of Sn and Nb on generalized stacking fault energy surfaces in zirconium and gamma hydride habit planes, Philos. Mag. A 91 (2011) 1665–1678.
[38] H.G. Kim, J.H. Baek, S.D. Kim, Y.H. Jeong, Microstructure and corrosion characteristics of Zr-1.5Nb-0.4Sn-0.2Fe-0.1Cr alloy with a beta-annealing, J. Nucl. Mater. 372 (2008) 304–311.
[39] R. Tewari, D. Srivastava, G.K. Dey, J.K. Chakravarty, S. Banerjee, Microstructural evolution in zirconium based alloys, J. Nucl. Mater. 383 (2008) 153–171.
[40] T.B. Britton, F.P.E. Dunne, A.J. Wilkinson, On the mechanistic basis of deformation at the microscale in hexagonal close-packed metals, P Royal Soc A 471 (2015) 20140881.
[41] H.L. Yang, Y. Matsukawa, S. Kano, Z.G. Duan, K. Murakami, H. Abe, Investigation on microstructural evolution and hardening mechanism in dilute ZrNb binary alloys, J. Nucl. Mater. 481 (2016) 117–124.
[42] C.D. Williams, R.W. Gilbert, Tempered structures of a Zr-2.5 wt % Nb alloy, J. Nucl. Mater. 18 (1966) 161–166.
[43] Y. Wei, Y. Li, L. Zhu, Y. Liu, X. Lei, G. Wang, Y. Wu, Z. Mi, J. Liu, H. Wang, Evading the strength–ductility trade-off dilemma in steel through gradient hierarchical nanotwins, Nat. Commun. 5 (3580) (2014) 1–8.
[44] X. Li, K. Lu, Playing with defects in metals, Nat. Mater. 16 (2017) 700–701.
[45] K. Lu, L. Lu, S. Suresh, Strengthening materials by engineering coherent internal boundaries at the nanoscale, Science 324 (2009) 349–352.
[46] S. Banerjee, S.J. Vijayakar, R. Krishnan, Strength of zirconium-titanium martensites and deformation behaviour, Acta Metall. 26 (1978) 1815–1831.
[47] X. Zhang, A. Misra, H. Wang, M. Nastasi, J.D. Embury, T.E. Mitchell, R.G. Hoagland, J.P. Hirth, Nanoscale-twinning-induced strengthening in austenitic stainless steel thin films, Appl. Phys. Lett. 84 (2004) 1096–1098.

[48] S. Ni, Y.B. Wang, X.Z. Liao, R.B. Figueiredo, H.Q. Li, S.P. Ringer, T.G. Langdon, Y.T. Zhu, The effect of dislocation density on the interactions between dislocations and twin boundaries in nanocrystalline materials, Acta Mater. 60 (2012) 3181–3189.

[49] Y.-H. Zhao, J.E. Bingert, X.-Z. Liao, B.-Z. Cui, K. Han, A.V. Sergueeva, A.K. Mukherjee, R.Z. Valiev, T.G. Langdon, Y.T. Zhu, Simultaneously increasing the ductility and strength of ultra-fine-grained pure copper, Adv. Mater. 18 (2006) 2949–2953.